Two-Phase Transport in Polymer Electrolyte Fuel Cells with Bilayer Cathode Gas Diffusion Media

Ugur Pasaogullari,[a,*] Chao-Yang Wang,[a,**,z] and Ken S. Chen[b,**]

[a]*Electrochemical Engine Center (ECEC), and Department of Mechanical and Nuclear Engineering, The Pennsylvania State University, University Park, Pennsylvania 16802, USA*
[b]*Engineering Sciences Center, Sandia National Laboratories, Albuquerque, New Mexico 87185-0834, USA*

A two-phase, full cell model based on the multiphase mixture (M^2) framework is developed to analyze the two-phase transport in polymer electrolyte fuel cells with bilayer cathode gas diffusion media (GDM), consisting of a coarse gas diffusion layer (GDL) with an average pore size around 10-30 μm and a microporous layer (MPL) with an average pore size ranging from 0.1 to 1 μm. Effects of the relevant properties of the MPL on liquid water transport are examined, including average pore size, wettability, thickness, and porosity. It is quantitatively shown that the MPL increases the rate of water back-flow across the membrane toward the anode by increasing the hydraulic pressure differential across the membrane, consequently reducing the net amount of water to be removed from the cathode. Furthermore, it is seen that different microporous and wetting characteristics of the MPL cause a discontinuity in the liquid saturation profile at the MPL-GDL interface, which in turn reduces the amount of liquid water in the catalyst layer-MPL interface. Our analyses show that the back-flow of liquid water increases with increasing hydrophobicity and thickness, and decreasing pore size and porosity of the MPL.
© 2005 The Electrochemical Society. [DOI: 10.1149/1.1938067] All rights reserved.

A main limitation in polymer electrolyte fuel cell (PEFC) performance results from the transport of reactants from the channel to the catalyst layer, referred to as the mass-transport limitation. This limitation is further amplified by the presence of liquid water, which blocks some of the open pores in the gas diffusion media (GDM) and thus reduces the available paths for the transport of reactant species. This phenomenon, commonly referred to as flooding, is more severe in the cathode because the slower oxygen reduction reaction (ORR) is more susceptible to the negative impact caused by flooding. Recently, a bilayer GDM, consisting of a coarse gas diffusion layer (GDL) and a finer microporous layer (MPL), has been employed by practitioners to reduce flooding in the porous cathode and to enhance water management in PEFCs by increasing the backflow tendency of liquid water across the membrane toward the anode. It has been shown that highly hydrophobic MPLs usually exhibit better performance.[1-13] Although the exact mechanisms are yet to be fully elucidated, the performance enhancement is usually associated with better water management capabilities of MPLs. In phosphoric acid fuel cells, Hara et al.[2] wetproofed the GDL using a fluorinated polyethylene film, which has much smaller pore size than commonly used polytetrafluoroethylene (PTFE) particles. It was found that this additional layer, which is similar to the MPL in PEFCs, improved oxygen reduction by reducing the flooding. Passalacqua et al.[3] also showed that introducing a hydrophobic layer between the carbon paper and the catalyst layer improves cell performance. The thin hydrophobic layer of about 2 mg/cm² of carbon (Vulcan XC-72), containing 40% of PTFE, substantially improved cell performance both in air and pure oxygen operation, by reducing the ohmic losses and increasing the limiting current density. Therefore, it was concluded that this thin hydrophobic layer is useful both in reducing cathode flooding and improving membrane humidification. Paganin et al.[4] found that the effect of the MPL thickness is more dominant than the PTFE content in improvement of polarization characteristics. Their experiments with pure oxygen, however, suggested that the performance improvement is largely due to decreased ohmic losses. Qi and Kaufman[5] discovered that MPLs reduced the performance differences among the different GDLs, and attributed this effect to improved water management. They have shown that MPLs are extremely useful, particularly when the GDL is prone to flooding. They observed that the MPL not only raised the limiting current density, but also improved membrane humidifica-

tion and hence reduced ohmic losses. They also analyzed the effect of PTFE content of MPL on cell performance, and concluded that, although the performances are very similar, the 45% PTFE content sublayer performed worst, while the 35% sublayer performed best, suggesting that there is an optimum for MPL hydrophobicity. They also noted that MPLs might improve the contact with the catalyst layer, thereby decreasing the contact losses. Kong et al.[6] found that adding pore formers to coatings applied on the GDL surface improves cell performance. They attributed the performance improvement to the fact that larger pores in MPL accumulate liquid water while the smaller pores remain free of liquid water, resulting in more effective transport of both gaseous oxygen and liquid water. Like Jordan et al.,[7] they also concluded that the pore size range on the order of a micrometer exhibited better performance than larger or smaller pores. It is likely due to a trade-off between water management and oxygen transport that with smaller pores water management is improved (though the oxygen diffusion is hindered), whereas with the larger pores the GDL becomes more prone to flooding.

It is evident from the experimental studies cited above that MPLs improve PEFC performance in several aspects. Two main causes of performance improvement are *(i)* enhancement of water management by improved humidification of the membrane at the anode side, hence decreasing the ohmic losses; and *(ii)* reduced flooding in the cathode, hence improved oxygen diffusion.

Although several studies exist on modeling of two-phase transport in PEFCs, only a few have discussed the effects of the MPL on water management and two-phase transport. Nam and Kaviany[14] have modeled the two-phase transport in multilayered cathode GDM using the unsaturated flow theory (UFT), which assumes a constant gas-phase pressure throughout, and which therefore neglects the gas flow counter to the liquid flow. They have optimized the MPL properties according to the total liquid water in the cathode GDM, and concluded that there exists an optimal MPL thickness and porosity. In contrast, Pasaogullari and Wang[15,16] elucidated the MPL effect using a full two-phase model, i.e., the multiphase mixture formulation commonly known as the M^2 model, in which the constant gas-phase pressure assumption is relaxed, thereby accounting for the gas flow in counter direction to the capillarity-induced liquid flow. Their results indicated for the first time that the build-up in liquid pressure in the cathode due to the presence of an MPL creates a hydraulic pressure differential to drive water flow back to the anode. This water back-flow can be controlled by pore size and MPL wettability, following the capillary flow theory developed by Pasaogullari and Wang.[17] In addition, the study of Pasaogullari and Wang revealed a capillarity-driven enhancement of oxygen transport once the two-

phase zone is formed. This new enhancement mechanism is, however, suppressed by the increase in the diffusion resistance, yielding an overall reduction in the oxygen transport capability in most cases of flooding. Weber and Newman[18] also mentioned the positive role played by MPL, which is to promote back-flow through the membrane by improving humidification of the membrane as well as the anode catalyst layer and by reducing the overall ohmic losses, hence improving PEFC performance. Reviews of other aspects of water transport in PEFCs are available in Ref. 19,20.

The aim of the present work is to develop a two-phase transport model based on the M^2 model for the entire polymer electrolyte membrane (PEM)-anode/cathode GDM assembly, and to analyze the liquid water transport in PEFCs with MPLs. Effects of MPL pore structure and wetting characteristics are also analyzed. Particularly, the effects of MPL properties on the net water transport rate across the membrane (a combined effect of electro-osmotic drag, back-diffusion, and hydraulic permeation) are analyzed. Net water transport across the membrane can only be analyzed with a model considering both anode and cathode as well as the membrane, an important feature that cannot be captured by half cell models (such as those in Ref. 14-16).

The present paper is organized as follows. A mathematical model for transport in the multilayered GDM and PEM is first presented based on the theory of liquid water flow in hydrophobic gas diffusion layers as put forth by Pasaogullari and Wang.[17] Then, liquid water transport with MPL is compared with the conventional PEFC configuration without MPL, and the effects of MPL properties are examined.

Mathematical Model

The present study focuses on liquid water transport in porous anode and cathode gas diffusion media and across the membrane. The cell is considered to be isothermal for simplicity. The gas channels are excluded from the modeling domain by designating the boundary conditions at the GDL/channel interfaces. Furthermore, catalyst layers are taken to be infinitely thin interfaces, and the anode hydrogen oxidation reaction (HOR) and cathode ORR are assumed to take place at the PEM-anode GDL and PEM-cathode GDM interfaces, respectively.

Under these assumptions, the modeling domain is defined to include the porous anode GDL, PEM, and cathode GDM, consisting of MPL and GDL, as shown in Fig. 1, along with the associated transport processes. Although the present model is developed in one dimension (i.e., in the through-plane direction), it can be readily implemented in a multidimensional computational fuel-cell dynamics (CFCD) model with the channel and catalyst layer incorporated, as illustrated in Ref. 21,22.

Two-phase water transport in gas diffusion media.— In this study, the M^2 model is employed to describe the two-phase transport processes in porous media. The M^2 model is an exact reformulation of the classical two-phase, two-fluid model into a single equation.[23,24] Unlike the unsaturated flow theory (UFT)[23] utilized in some of the earlier two-phase PEFC models,[14,18,25,26] the M^2 formulation does not require a constant gas-phase pressure assumption across the porous medium; hence, it also accounts for the gas flow counter to the capillarity-driven liquid flow. Interested readers are referred to Wang and Cheng[23] for details of the M^2 model and its applications to a number of multiphase transport problems in porous media.

Mass conservation in steady state for the two-phase mixture as given by the M^2 formulation is

$$\frac{d(\rho \mathbf{u})}{dx} = 0 \qquad [1]$$

where $\mathbf{u}$ is the superficial mixture velocity based on the total volume of the porous medium and ρ is the mixture density, given as[23]
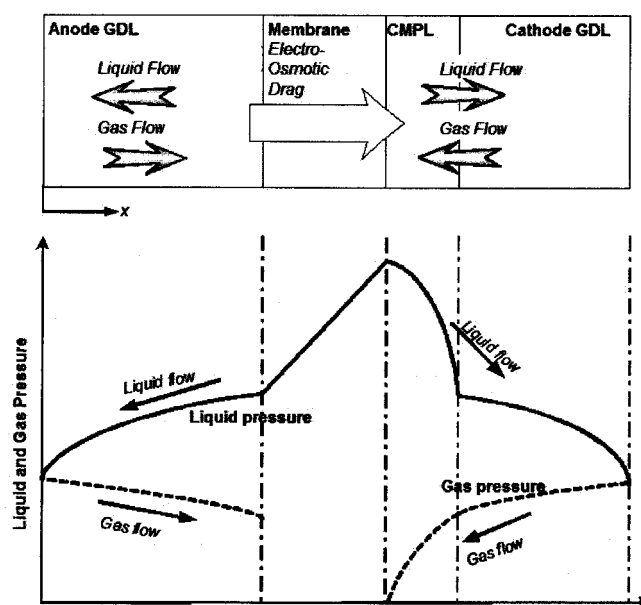
$$\rho = \rho_l s + \rho_g (1 - s) \qquad [2]$$

Figure 1. Schematics of modeling domain, transport phenomena, and individual phase pressure profiles in a PEFC with microporous layer.

Here, s and $(1 - s)$ represent the fraction of the open pore space occupied by the liquid and gas phases, respectively. When Eq. 1 is integrated along the GDM thickness

$$\rho \mathbf{u} = \mathbf{j}_m \qquad [3]$$

Here, $\mathbf{j}_m$ indicates the total mass flux through the porous media in both phases, and corresponding expressions for each individual layers are given in Table I.

The steady-state, one-dimensional species conservation equation of the M^2 formulation, when written in terms of molar concentrations, is[22]

$$\frac{d}{dx}(\gamma_c^i \mathbf{u} C^i) = \frac{d}{dx}\left(D_g^{i,eff}\frac{d}{dx}C_g^i\right) - \frac{d}{dx}\left[\left(\frac{mf_l^i}{M^i} - \frac{C_g^i}{\rho_g}\right)\mathbf{j}_l\right] \qquad [4]$$

where the advection correction factor, γ_c, is

$$\gamma_c^i = \begin{cases} \dfrac{\rho}{C^{H_2O}}\left(\dfrac{\lambda_l}{M^{H_2O}} + \lambda_g \dfrac{C_g^{H_2O}}{\rho_g}\right) & \text{for water} \\[2ex] \dfrac{\rho \lambda_g}{\rho(1 - s)} & \text{for other species} \end{cases} \qquad [5]$$

In Eq. 4, C^i denotes the total molar concentration of species i in liquid and gas phases, and is defined as

$$C^i = (1 - s)C_g^i + sC_l^i \qquad [6]$$

The gas-diffusion coefficient, $D_g^{i,eff}$ is corrected for tortuosity and reduction in the open pore space due to presence of liquid water via Bruggeman correlation,[27] *e.g.*

$$D_g^{i,eff} = [\varepsilon(1 - s)]^{1.5}D_g^i \qquad [7]$$

Table I. Mass and water flux for individual layers of PEFC.

	Mass flux, $\mathbf{j}_m$ (Eq. 3)	Water molar flux, $\mathbf{j}_w$ (Eq. 15 and 24)
Anode GDL	$I/F(M^{H_2}/2 + \alpha M^{H_2O})$	$I/F\alpha$
Membrane	N/A	$I/F\alpha$
Cathode GDL/MPL	$I/F[-M^{O_2}/4 + (\alpha + 1/2)M^{H_2O}]$	$I/F(\alpha + 1/2)$

Note that Eq. 4 strongly resembles the single-phase species conservation except for the last term, which describes the capillary transport of species. This equation reduces to its counterpart of single-phase species equation when liquid saturation, s, approaches zero or unity. Note that, unlike the UFT approximation, the capillary transport term also accounts for the variation in gas-phase pressure through the porous media; hence, the gas flow in the counterdirection to the capillarity-induced liquid flow is considered in transport of species. Due to small length scales involved in PEFCs, effect of gravity is negligible and hence the liquid flux, $\mathbf{j}_l$, is given by

$$\mathbf{j}_l = \frac{\lambda_l \lambda_g}{\nu} K \nabla p_c \qquad [8]$$

where λ_l and λ_g are relative mobilities of gas and liquid phases, respectively

$$\lambda_k = \frac{k_{rk}/\nu_k}{\sum_k k_{rk}/\nu_k} \qquad [9]$$

and ν is the kinematic viscosity of the two-phase mixture

$$\nu = \left[\sum_k \frac{k_{rk}}{\nu_k} \right]^{-1} \qquad [10]$$

Here, we assume that the GDL and MPL are isotropic and homogeneous porous media, and the relative permeabilities of individual phases are assumed to be proportional to the cube of individual phase saturations, i.e.

$$k_{rk} = s_k^3 \qquad [11]$$

The capillary pressure is the difference between the pressures of wetting and nonwetting phases

$$p_c = p_g - p_l \qquad [12]$$

In this work, we relate the capillary pressure to individual phase saturations via a Leverette function, $J(s)$[23]

$$p_c = \sigma \cos(\theta_c) \left(\frac{\varepsilon}{K} \right)^{1/2} J(s) \qquad [13]$$

where $J(s)$ is the Leverette function, and given as[16,17]

$$J(s)$$
$$= \begin{cases} 1.417(1-s) - 2.120(1-s)^2 + 1.263(1-s)^3 & \text{if } \theta_c < 90° \\ 1.417s - 2.120s^2 + 1.263s^3 & \text{if } \theta_c > 90° \end{cases}$$
$$[14]$$

Note that, for a hydrophilic media, the wetting phase is the liquid phase; therefore, the Leverette function is expressed in terms of gas-phase saturation, whereas in hydrophobic media the gas phase becomes the wetting phase and therefore the liquid-phase saturation is used. Contact angle, θ_c of the GDL is dependent upon hydrophilic $(0° < \theta_c < 90°)$ or hydrophobic $(90° < \theta_c < 180°)$ nature of the GDM and varies with the Teflon content. Here, the surface tension σ, for the liquid water-air system is taken as 0.0625 N/m at 80°C.

Mass fraction of water in liquid phase (mf_l^i) is unity, since solubility of other species in liquid phase is assumed to be zero. Therefore, integration of Eq. 4 for water species across the GDM thickness yields

$$\gamma_c^{H_2O} \mathbf{u} C^{H_2O} - D_g^{H_2O,eff} \nabla C_g^{H_2O} + \left(\frac{1}{M^{H_2O}} - \frac{C_g^{H_2O}}{\rho_g} \right) \mathbf{j}_l = \mathbf{j}_w \quad [15]$$

Here, $C_g^{H_2O}$ is the molar concentration of water in the gas phase and is equal to saturation concentration of water (i.e., $P_{sat}/R_u T$) if the gas is fully saturated with water vapor; $\mathbf{j}_w$ represents the net molar flux of water through individual layers of the cell and has the units of [mol m^{-2} s^{-1}]. For each individual layer, $\mathbf{j}_w$ is a function of local current density through the production and net water transport

across the membrane, α. Here, the net water transport coefficient across the membrane is defined as the net number of water molecules transported across the membrane per proton, such that

$$j_m^{H_2O} = \alpha \frac{I}{F} \qquad [16]$$

The corresponding expressions for the net water flux for each component of the cell are given in Table I.

The liquid saturation is expressed in terms of the total water concentration via the following relation

$$s = \frac{C^{H_2O} - C_{sat}^{H_2O}}{C_l^{H_2O} - C_{sat}^{H_2O}}, \quad \text{where } C_l^{H_2O} = \frac{\rho_l}{M^{H_2O}} \qquad [17]$$

Once the liquid saturation, s, is obtained, the individual phase velocities are obtained using the following relations

$$\rho_l \mathbf{u}_l = \mathbf{j}_l + \lambda_l \rho \mathbf{u} \qquad [18]$$

$$\rho_g \mathbf{u}_g = -\mathbf{j}_l + \lambda_g \rho \mathbf{u} \qquad [19]$$

Then, the phase pressure drops can be obtained using Darcy's law for each individual phase k

$$\nabla p_k = - \frac{\mu_k}{k_{rk} K} \mathbf{u}_k \qquad [20]$$

Water transport across the membrane.— In this study, we consider the water transport across the membrane by permeation driven by the hydraulic pressure gradient, by diffusion due to water concentration gradient across the membrane, and by electro-osmotic drag due to proton flux. These three modes of water transport, namely hydraulic permeation, diffusion, and electro-osmotic drag, are described with the following equation

$$\frac{d}{dx} \left(-\rho_l \frac{K_m}{\mu_l M^{H_2O}} \frac{d}{dx} p_l \right) = \frac{d}{dx} \left(D_m^{H_2O} \frac{d}{dx} C_m^{H_2O} \right) - \frac{d}{dx} \left(n_d \frac{I}{F} \right) \quad [21]$$

where the membrane water concentration, $C_m^{H_2O}$, is

$$C_m^{H_2O} = \lambda \frac{\rho_{dry}}{EW} \qquad [22]$$

Here, λ is the number of water molecules per sulfonate group in the membrane and is referred to as the water content of the membrane. The thermodynamic equilibrium of the membrane water content with the surrounding medium is described by the water uptake curve. Zawodzinski et al.[28] measured the water uptake for Nafion membranes, concluding that the water content of the membrane is around 16 when it is in equilibrium with liquid water at 80°C, and the relation between the water content of the membrane and the surrounding medium water activity, $a(P_g^{H_2O}/P_{sat})$, is given by the water uptake curve when the membrane is humidified with water vapor. Here, we use a third-order polynomial curve fit to Zawodzinski et al.'s data to calculate membrane water content when the membrane is in equilibrium with water vapor

$$\lambda = 1.4089 + 11.263a - 18.768a^2 + 16.209a^3 \quad \text{for a} \leqslant 1$$
$$[23]$$

In Eq. 21, K_m, $D_m^{H_2O}$, and n_d denote membrane hydraulic permeability, water diffusivity, and electro-osmotic drag coefficient, respectively. When integrated along the membrane thickness in steady state, Eq. 21 becomes

$$-\rho_l \frac{K_m}{\mu_l M^{H_2O}} \frac{d}{dx} p_l - D_m^{H_2O} \frac{d}{dx} C_m^{H_2O} + n_d \frac{I}{F} = \mathbf{j}_w \qquad [24]$$

The reported values in the literature for hydraulic permeability of membrane show a large variation, namely between 1.8 $\times 10^{-18}$ m^2 [29] and 2×10^{-20} m^2,[30] for Nafion-based membranes humidified with liquid water. In this work, we use the datum from

Ref. 30, which is 2×10^{-20} m^2 for a membrane fully humidified with liquid water at 80°C (i.e., $\lambda = 16$).

Here, the diffusion coefficient of water in the membrane is taken from Motupally et al.,[31] and is given as (m^2/s)

$$D_m^w = \begin{cases} 3.1 \times 10^{-7}\lambda(e^{0.28\lambda} - 1)e^{-2346/T} & 0 < \lambda \leq 3 \\ 4.17 \times 10^{-8}\lambda(1 + 161e^{-\lambda})e^{-2346/T} & 3 < \lambda \leq 17 \end{cases}$$

$$[25]$$

It is known that the electro-osmotic drag of water is linearly proportional to the number of protons transported across the membrane; this proportionality constant is called the electro-osmotic drag coefficient and known to be a function of water content of the membrane.[32,33] Springer et al.[32] used a linear dependence of electro-osmotic drag on water content ($2.5\lambda/22$), whereas Zawodzinski et al.[33] have shown that the electro-osmotic drag coefficient is around 2.5 when the membrane is humidified with liquid water and around unity when humidified with water vapor. That is

$$n_d = \begin{cases} 1 & \lambda \leq 10.1129 \text{ (vapor equilibriated)} \\ 2.5 & \lambda = 16 \text{ (liquid equilibriated)} \end{cases}$$

$$[26]$$

Boundary conditions.— In our one-dimensional modeling domain ranging from the anode GDL to cathode GDL, the boundary conditions are only required at two GDL/channel interfaces. For a flooded GDL, this boundary condition depends on the size, shape, and number of the liquid droplets covering the GDL surface, and is thus a function of such parameters as the channel gas velocity and GDL surface wettability. However, in this work we assume that in both anode and cathode, the GDL surface facing the gas channel is free of liquid water. Although this assumption is an approximation, it is valid for high channel gas velocities and/or carbon cloth GDL, according to a recent visualization study.[34] Therefore, liquid water is assumed to evaporate at the GDL surface and the water vapor is transported from the GDL to the gas channel by convective mass transfer.

$$C^{H_2O}\big|_{ACh-AGDL} = C_{ACh}^{H_2O} - \frac{\alpha}{h_m}\frac{I}{F}$$

$$[27]$$

$$C^{H_2O}\big|_{CCh-CGDL} = C_{CCh}^{H_2O} + \frac{1}{h_m}\left(\alpha + \frac{1}{2}\right)\frac{I}{F}$$

$$[28]$$

The convective mass-transfer coefficient, h_m, is calculated by the heat/mass-transfer analogy as outlined in Ref. 17,24

$$h_m = Nu_D\frac{Sc}{Pr} \cdot \frac{D^i}{d_h}$$

$$[29]$$

where D^i is the diffusion coefficient of species i, and d_h is the hydraulic diameter of the gas channel.

Numerical procedure.— The present model is solved separately in three different regions, namely anode GDL, PEM, and cathode GDM, simultaneously. As seen in Table I, the water fluxes across these layers are functions of the net water transport coefficient, α, which is initially unknown. Therefore, an iterative procedure is used to determine α. An initial guess is provided for α, and this guess is improved in consecutive iterations using the bisection method until phase pressures and water content of the membrane converge to the same value at the interfaces. A relative error margin of 10^{-7} is set for convergence criteria, which requires around 25 iterations to obtain α accurate up to seven digits. The resulting governing equations of water transport are nonlinear first-order ordinary differential equations, which are solved using a fourth-order adaptive-step Runge-Kutta method.

Results and Discussion

Effects of MPL.— In this section, we compare water distribution and flow across the PEFC in two different configurations in order to investigate the effect of MPL. The first configuration is a conven-

Table II. Material properties, transport parameters, and operating conditions.

Parameter	Value
Transport parameters	
Surface tension, σ^a	0.0625 N/m
Anode gas kinematic viscosity, $\nu_{g,a}{}^a$	1.11×10^{-5} m^2/s
Cathode gas kinematic viscosity, $\nu_{g,c}{}^a$	1.76×10^{-5} m^2/s
Liquid kinematic viscosity, $\nu_l{}^a$	3.52×10^{-7} m^2/s
Liquid density, $\rho_l{}^a$	974.85 kg/m^3
Water vapor diffusivity in anode at 1.5 atm, 353.15 K, $D_{g,a}^{H_2O}$	$1.273 \cdot 10^{-4}$ m^2/s
Water vapor diffusivity in cathode at 1.5 atm, 353.15 K $D_{g,c}^{H_2O}$	$2.625 \cdot 10^{-5}$ m^2/s
Prandtl number in anode, Pr_a	0.650
Prandtl number in cathode, Pr_c	0.739
Schmidt number in anode, Sc_a	0.261
Schmidt number in cathode, Sc_c	0.532
Hydraulic diameter of channel, d_h	1.0 mm
Nusselt number, $Nu_D{}^a$	3.61
Material properties (Typical values)	
GDL absolute permeability, K_{GDL} (Toray TGPH-120)^b	8.69×10^{-12} m^2
GDL porosity, $\varepsilon_{GDL}{}^b$	0.75
GDL contact angle, θ_c (wet-proofed)	110°
Anode GDL thickness, δ_{AGDL}	300 μm
Total cathode gas diffusion media thickness, δ_C	300 μm
Membrane thickness (Nafion 111), δ_{mem}	25.4 μm
Membrane hydraulic permeability, K_{mem} (at $\lambda = 16$)^c	2×10^{-20} m^2
Baseline-case MPL properties	
Thickness, δ_{MPL}	30 μm
Porosity, ε_{MPL}	0.5
Average pore size, d_{MPL}	250 nm
Absolute permeability, K_{MPL}	2.47×10^{-16} m^2
Contact angle, $(\theta_c)_{MPL}$	120°
Operating conditions	
Cell temperature, T	353.15 K
Anode channel pressure, p_A	1.5 atm
Cathode channel pressure, p_C	1.5 atm
Anode channel humidity	100%
Cathode channel humidity	100%

^{a} Reference 37.
^{b} Reference 38.
^{c} Reference 30.

tional PEFC without MPL. The properties of the materials for this configuration are given in Table II. In the other configuration, an MPL with baseline properties as given in Table II is added to the cathode GDL, resulting in a bilayer cathode GDM. Here, the total cathode GDM thickness is kept constant at 300 μm, with or without MPL. Both the anode and cathode GDL properties are selected to represent carbon paper (Toray-TGPH-120), as given in Table II.

In Fig. 2, the variation in the net water transport coefficient with the current density is given for two membrane thicknesses, Nafion 111 (25.4 μm) and Nafion 112 (50.8 μm). When, α (as defined in Eq. 16) is positive, the electro-osmotic drag of water is larger than hydraulic permeation and back-diffusion of water across the membrane; hence, the net water transport across the membrane is toward the cathode.

When an MPL is added to the cathode GDM, it is seen that water flux toward the anode by hydraulic permeation is significantly increased, particularly at lower current densities. Due to its smaller pore size and higher hydrophobicity, the MPL has much larger cap-
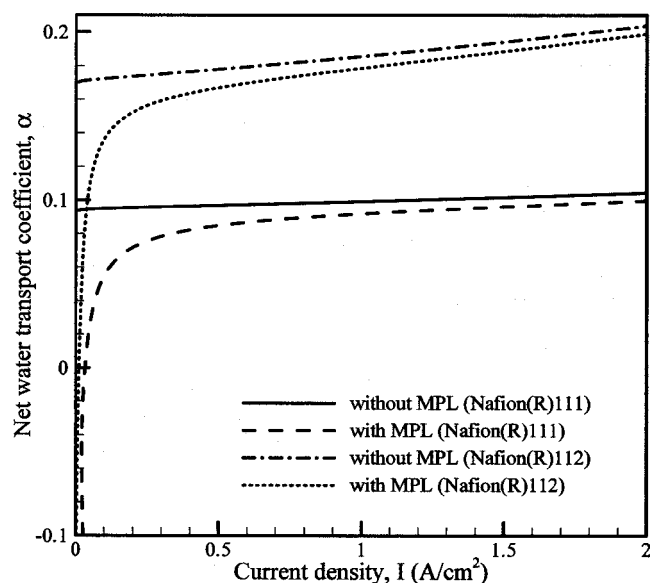
Figure 2. Net water transport coefficient, α with and without MPL for two different membrane thicknesses. MPL properties are taken from the baseline case given in Table II.

Figure 3. Effect of MPL on (a) liquid pressure; and (b) liquid saturation across the cathode GDM.

illary pressure and hence increases the liquid pressure on the cathode side of the membrane. Here, the permeability of the MPL is calculated from the following expression given by Rumpf and Gutte[35] for packed beds with a narrow range of size distribution:

$$K = \frac{\varepsilon^{5.5}}{5.6}d^2 \qquad [30]$$

where d is the average pore diameter. For an MPL having an average pore size of 0.25 μm and a porosity of 0.5, this expression gives a permeability of 0.25×10^{-15} m^2, compared to 8.7×10^{-12} m^2 for a carbon-paper GDL. This smaller permeability causes much higher liquid pressure gradient across the cathode GDM as shown in Fig. 3a, which in turn increases the hydraulic pressure differential across the membrane and hence the water flux across the membrane due to permeation. The higher water permeation flux from the cathode to the anode consequently lowers the net water transport coefficient through the membrane. At higher current densities, the electro-osmotic drag dominates over the enhanced hydraulic permeation; therefore, the effect of MPL is not as significant as at low current densities.

It is evident from Fig. 2 that the net water transport coefficient increases with increasing membrane thickness. This is because the electro-osmotic drag does not depend on the membrane thickness, while both the back-diffusion and hydraulic permeation are inversely proportional to the membrane thickness.

Figure 3a shows the liquid pressure profiles across the cathode GDM, where the gas pressure in cathode channel is 1.5 atm. It is seen that the increase in liquid pressure across the GDM without MPL is very small, thus not providing sufficient pressure gradient across the membrane to enhance water transport by permeation from the cathode to the anode. However, with the baseline-case MPL, the pressure differential increases by more than 80 kPa at a current density of 1.5 A/cm^2.

In Fig. 3b, the liquid saturation profiles across the cathode GDM are shown. It is seen that the maximum liquid saturation is less than 10%, which does not introduce severe effects of flooding, due to the boundary condition utilized here (0% liquid saturation at the GDL-channel interface). It is seen that, with a single-layer GDL, the liquid saturation is a continuous profile from the cathode channel-GDL interface to the cathode GDL-catalyst layer interface. However, for the bilayer GDM with MPL, there is a discontinuity at the GDL-
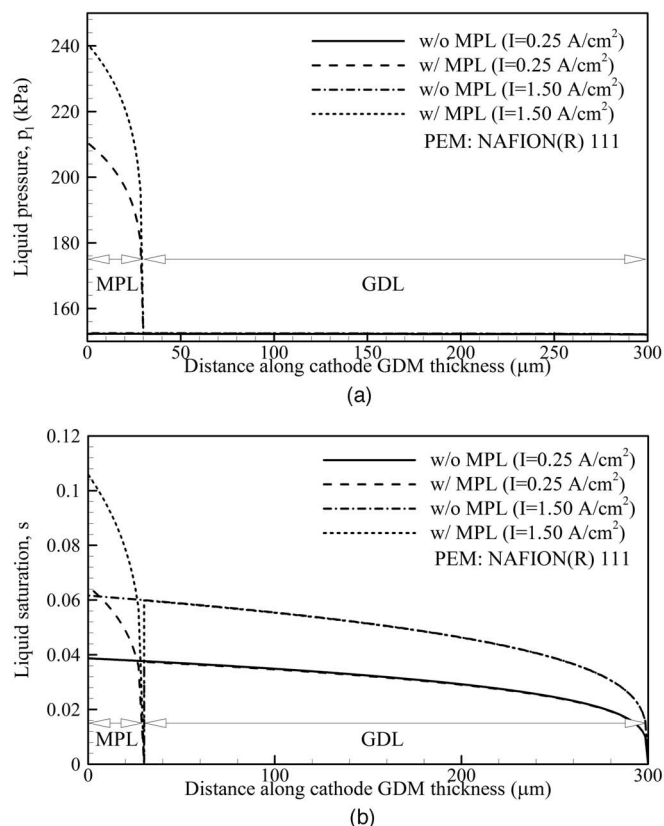
MPL interface due to the disparity in the porous and wetting characteristics of MPL and GDL. This discontinuity is best explained by an illustration of capillary pressure *vs* liquid saturation for both GDL and MPL, as shown in Fig. 4. Since both gas- and liquid-phase pressures are continuous across the interface; the capillary pressure is also continuous, thus leading to
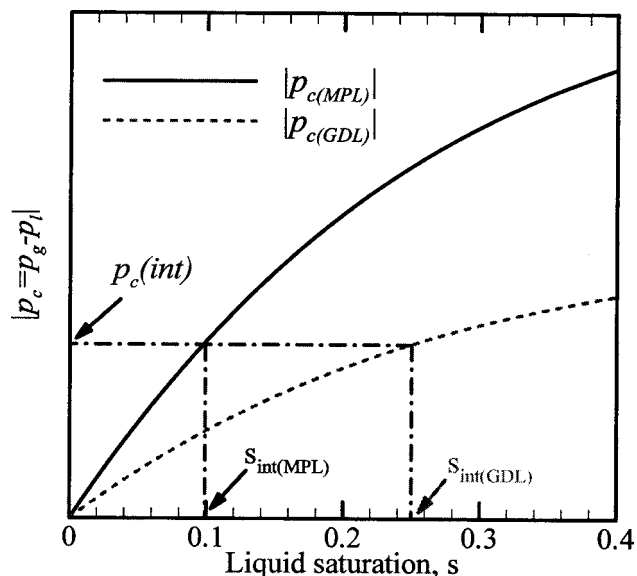

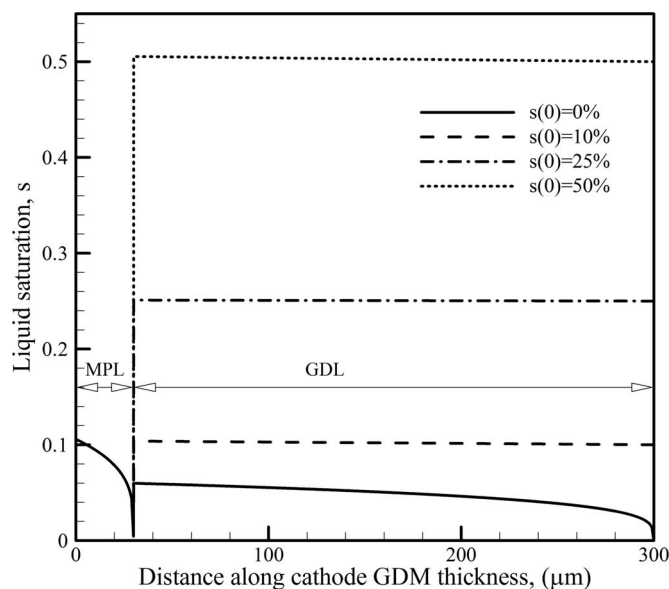**Figure 4.** Schematics of saturation discontinuity at the GDL-MPL interface.

Figure 5. Liquid saturation profiles with different boundary conditions at the GDL/channel interface.

$$\cos(\theta_c^{GDL})\left(\frac{\varepsilon^{GDL}}{K^{GDL}}\right)^{1/2}J(s_{int}^{GDL}) = \cos(\theta_c^{MPL})\left(\frac{\varepsilon^{MPL}}{K^{MPL}}\right)^{1/2}J(s_{int}^{MPL})$$

$$[31]$$

Due to its larger permeability, under the same capillary pressure, the liquid saturation is much higher for coarse GDL than for MPL; hence, at the interface the MPL has much lower saturation than GDL. However, again due to smaller permeability, increase in the liquid saturation is much faster across the MPL, and in some cases (such as those shown in Fig. 3b) the liquid saturation value at the cathode GDM-catalyst layer interface may exceed the single-layer value. In cases where the liquid saturation value at the GDL-channel interface is not equal to zero, as in Fig. 5, the MPL has an additional advantage of reducing the liquid saturation at the cathode GDM-catalyst layer interface.

In Fig. 6a and b, the hydraulic pressure differential across the membrane is plotted against the distance along the membrane thickness for Nafion 111 and Nafion 112 membranes, respectively. It is seen that the hydraulic pressure differential across the MPL can be increased as high as 80 kPa by MPL, thereby improving the permeation of water from cathode to anode. When the net water transport coefficient is positive, the electro-osmotic drag overcomes the back-flow of water; hence, the anode loses water. By comparing the molar ratio of water loss to H_2 consumption in the anode to the molar ratio of water to H_2 in the fully humidified anode feed (i.e., 100% RH at 80°C and 1.5 atm gas pressure), there is a possibility of water condensation in the anode. However, the flooding thus caused is negligibly small as compared to that occurring in the cathode. Therefore, the water concentration in the bulk of the anode gas channel has been assumed to be at saturation; consequently, the anode side of the membrane is assumed to be in equilibrium with water vapor in our calculations. Because the cathode side is flooded, the membrane is in equilibrium with liquid water on the cathode side. Note that there is water transport across the membrane via permeation (due to the hydraulic pressure differential) only where the membrane is in equilibrium with liquid water with a corresponding water content, λ, of 16. Furthermore, the water content is uniform in the membrane region hydrated with liquid water; thus, water diffusion in membrane only occurs in regions which have a gradient in water content. This leads to a water content profile with discontinuous slopes across the
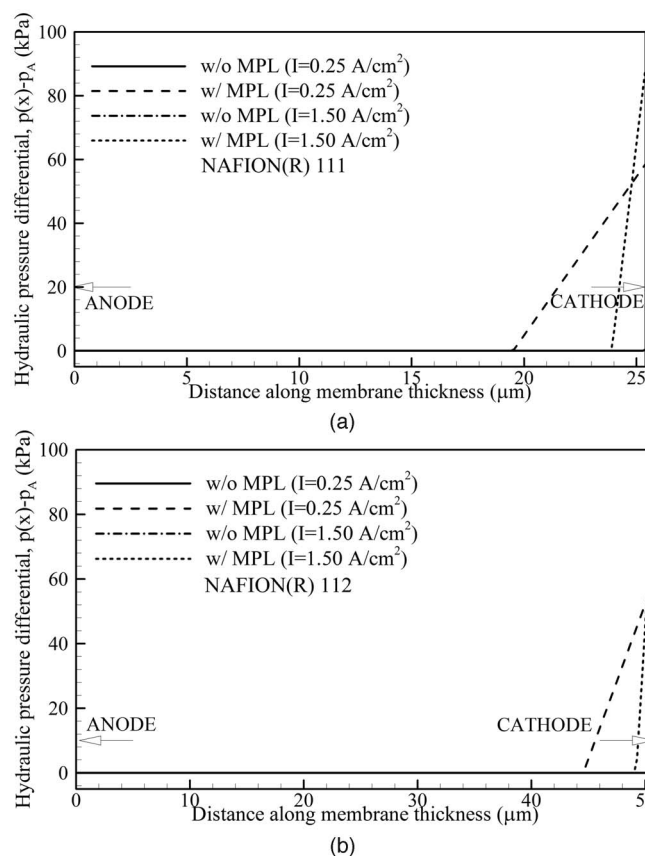

Figure 6. Hydraulic pressure profiles in the membrane for (a) Nafion 111 (25.4 μm) and (b) Nafion 112 (50.8 μm).

membrane as shown in Fig. 7a and b, once there is liquid water on the cathode side of the membrane and the anode side is under humidified.

In Fig. 7a and b, it is seen that the region of the membrane that is in equilibrium with liquid water ($\lambda = 16$) is extended by using MPL, increasing overall water content of the membrane for both membrane thicknesses. However, it is seen that in the thinner membrane (*e.g.*, Nafion 111), a relatively larger portion of the membrane is in equilibrium with liquid water, so the average water content of the thinner membrane is higher. It is also seen that, with the increasing current density, this liquid water equilibrated region becomes smaller.

It is observed that a bilayer cathode GDM consisting of an MPL and a coarse GDL results in water transport characteristics similar to those achieved by adjusting the operating conditions, such as higher cathode and lower anode pressures. Particularly, operating with pressure differentials has been shown to significantly improve the performance,[8,13,36] particularly due to improvement of membrane water content, as provided by MPL. In all these cases, an increased pressure differential across the membrane ensues, which enhances the back-flux (i.e., toward the anode) of water.

Effect of MPL thickness.— In this section, we analyze the effects of the MPL thickness on water transport and distribution. The parameters used for this case are the same as those in Table II, except that the thicknesses of the MPL and GDL are varied in order to keep the total thickness of the cathode GDM to 300 μm. As seen in Fig. 8, the net water transport coefficient is a strong function of MPL thickness, particularly at lower current densities. As the MPL thickness increases, the net water transport coefficient curve shifts downward, indicating that the water flux toward the anode is increasing. With increasing MPL thickness, the resistance to liquid
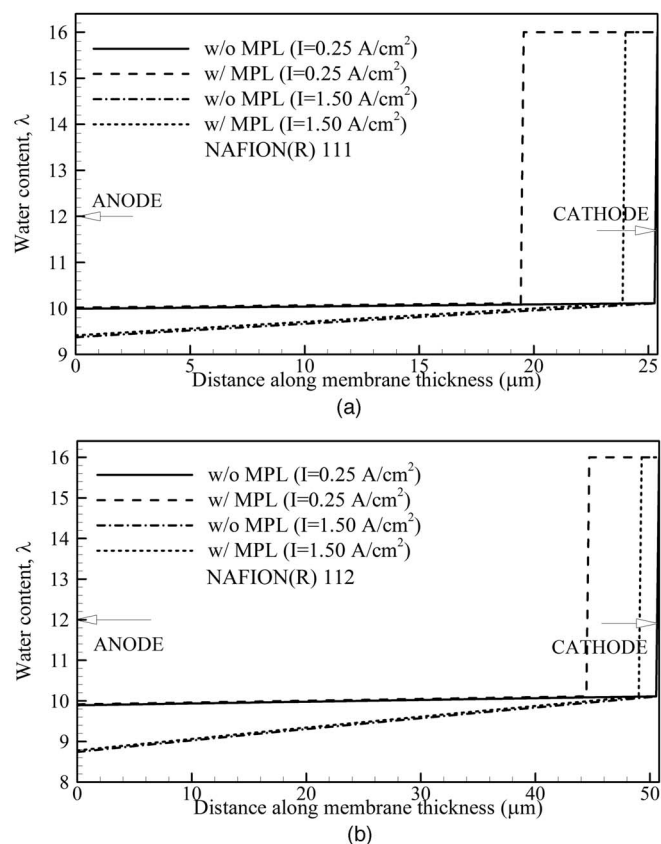
Figure 7. Water content profiles in the membrane for (a) Nafion 111 (25.4 μm) and (b) Nafion 112 (50.8 μm).
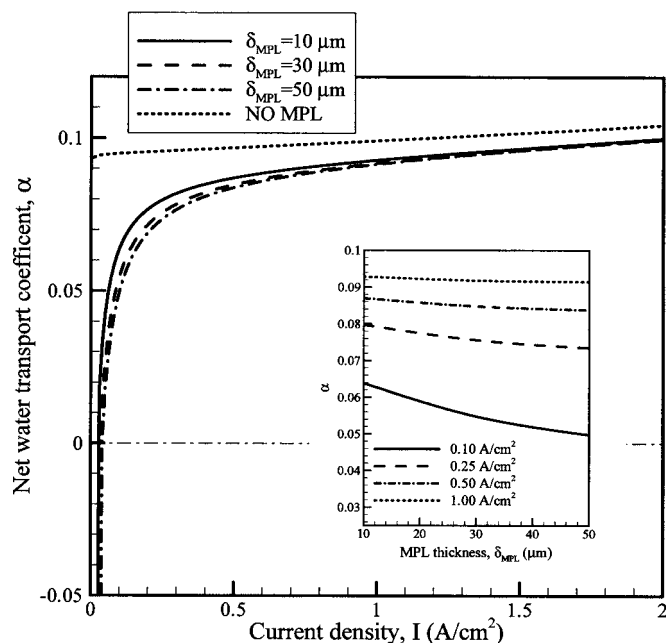

Figure 8. Net water transport coefficient, α, for different MPL thicknesses. Other MPL properties are taken from baseline case given in Table II. Inset shows the variation of net water transport coefficient with MPL thickness at different current densities.

Figure 9. Liquid pressure profiles in cathode GDM for different MPL thicknesses at 1.5 A/cm². Other MPL properties are taken from baseline case given in Table II. Inset shows the variation of net water transport coefficient with MPL thickness at different current densities.
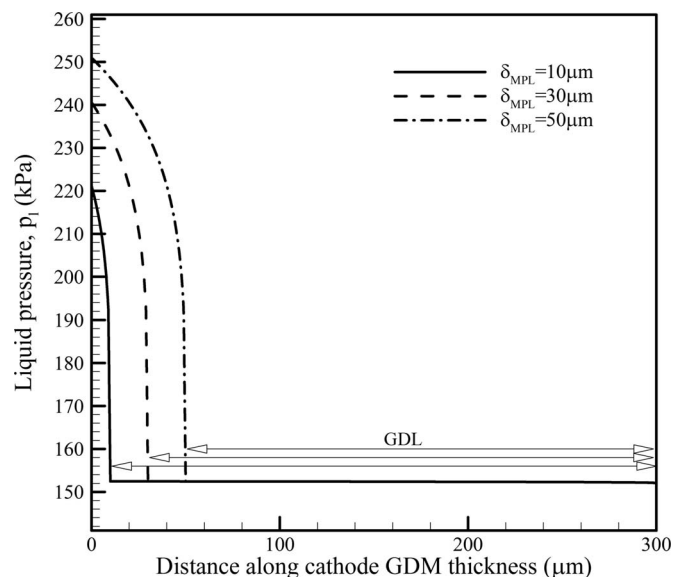
water flow in the cathode increases, and this increased resistance causes the fraction of water flowing through the membrane toward the anode to increase, resulting in a decrease in the cathode water flux. The inset of Fig. 8 shows the change of net water transport coefficient with the MPL thickness at several current densities. It is seen that the dependence of net water transport coefficient on the MPL thickness is much stronger at lower current densities, largely due to weaker electro-osmotic drag. At higher current densities, the electro-osmotic drag dominates over the hydraulic permeation, and the effect of the MPL thickness decreases.

The liquid pressure profiles for different MPL thicknesses at a current density of 1.5 A/cm² are shown in Fig. 9. As discussed above, due to smaller permeability of MPL, there is a larger increase in liquid pressure in the MPL; hence, with increasing MPL thickness, the liquid water pressure at the cathode side of the membrane increases. This causes a higher hydraulic pressure differential across the membrane, resulting in the increased water flux toward the anode.

Effect of MPL pore size.— Figure 10 shows the net water transport coefficient across the membrane for several mean pore sizes of MPL. Here, the properties of the MPL except for the mean pore size are taken from the baseline case, which are given in Table II. The net water transport curve shifts downward with decreasing mean pore size, indicating increasing water flux toward the anode. The capillary pressure and hence the liquid water pressure in the MPL increase with decreasing pore size. Further, the MPL permeability decreases with decreasing pore size (see Eq. 30), which increases resistance to water flow toward the cathode channel. Therefore, water tends to flow in the path which has smaller resistance, increasing the flow rate toward the anode. The MPL pore size effect is much more visible at lower current densities, in which the back-flux of water dominates over the electro-osmotic drag. As the current density increases, the electro-osmotic drag of water across the membrane becomes larger, diminishing the effect of MPL. As seen in the inset of Fig. 10, the mean pore size of MPL is not very effective at higher current densities.

It is evident that smaller MPL pore size increases the tendency of liquid water flow toward the anode. However, a design with the smallest pore size may not be optimal since the gas phase transport will be hampered with decreasing pore sizes. Therefore, the optimal
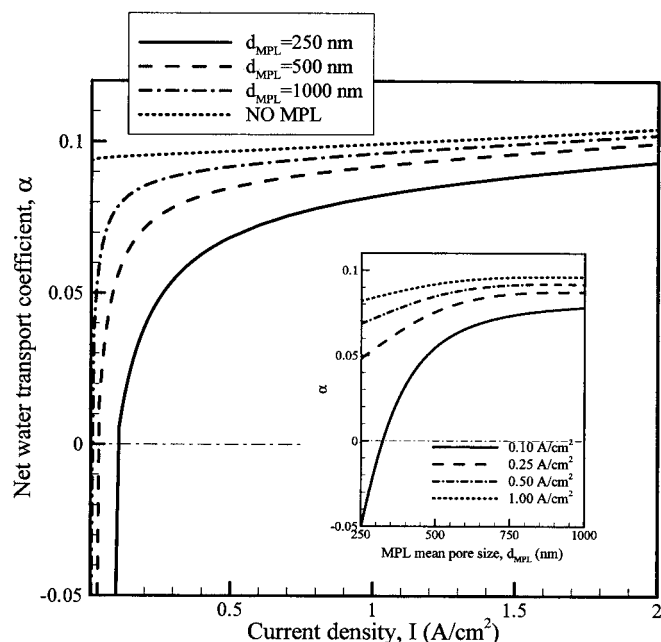
Figure 10. Net water transport coefficient, α, for different mean pore sizes of MPL. Other MPL properties are taken from baseline case given in Table II. Inset shows the variation of net water transport coefficient with mean pore size of MPL at different current densities.

Figure 12. Net water transport coefficient, α, for different MPL contact angles. Other MPL properties are taken from baseline case given in Table II. Inset shows the variation of net water transport coefficient with MPL contact angles at different current densities.

MPL pore size should be governed by the competing effects of water transport and oxygen diffusion, and both have to be considered in optimizing the MPL structure.

Effect of MPL porosity.— Figure 11 shows the net water transport coefficient with respect to current density for different MPL porosities. As seen in Fig. 11, the MPL porosity is also quite effective in controlling the water transport in a PEFC. With decreasing
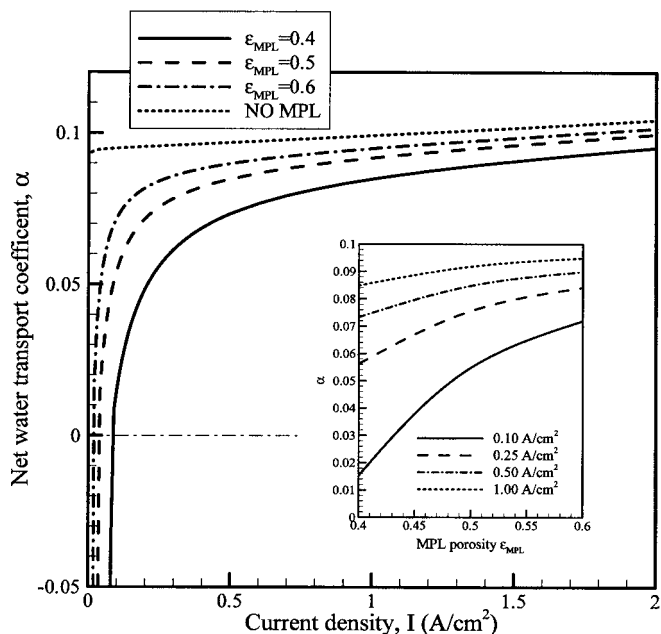
MPL porosity, resistance to the liquid water flow in the cathode increases, which results in increased water flux toward the anode, as indicated by lowering of the net water transport coefficient shown in Fig. 11. The inset of Fig. 11 shows the change in the net water transport with MPL porosity at different current densities. It is clearly seen that the effect of MPL porosity is more dominant at lower current densities, since electro-osmotic drag is not dominant at these current densities. This behavior shows a similarity to the effect of MPL pore size, which determines the absolute permeability.

Effect of MPL wettability.— As with the porosity and the pore size, the wetting characteristics of the MPL also affect the water transport in PEFCs. Capillarity is directly linked to wettability of the porous materials. In this work, we characterize the MPL wettability by an average contact angle, and we analyze the effect of this average contact angle. Figure 12 shows the net water transport coefficient for different MPL contact angles. It is seen that as the MPL contact angle increases (i.e., more hydrophobic), permeation of water across the membrane toward the anode due to hydraulic pressure differential is enhanced, resulting in a lower net water transport coefficient. As shown in the inset of the same figure, the slope of the curve decreases with increasing current density, as electro-osmotic drag is more effective in higher current densities. It is evident from Eq. 13 that the capillary pressure is a linear function of $\cos(\theta_c)$. When the MPL is less hydrophobic (i.e., lower contact angle), the liquid pressure build-up in the MPL is smaller, resulting in a smaller liquid pressure at the cathode side of the membrane. Consequently, the water flux toward the anode is smaller. Also note that, with increasing MPL contact angle, the capillary transport of liquid water across the MPL is facilitated; therefore, the liquid saturation rise across the MPL is reduced.

In the analysis of the effect of MPL wettability, we have not accounted for the fact that the mean pore size also varies with MPL wettability. Because the PTFE and carbon particles in the MPL differ significantly in size, the mean pore size of the MPL also depends on the PTFE content, hence wettability. This effect has to be considered for more accurate analysis and optimization of MPL. However, in general it can be said that the MPL provides better water management capabilities with higher hydrophobicity.

Figure 11. Net water transport coefficient, α, for different MPL bulk porosities. Other MPL properties are taken from baseline case given in Table II. Inset shows the variation of net water transport coefficient with MPL bulk porosity at different current densities.
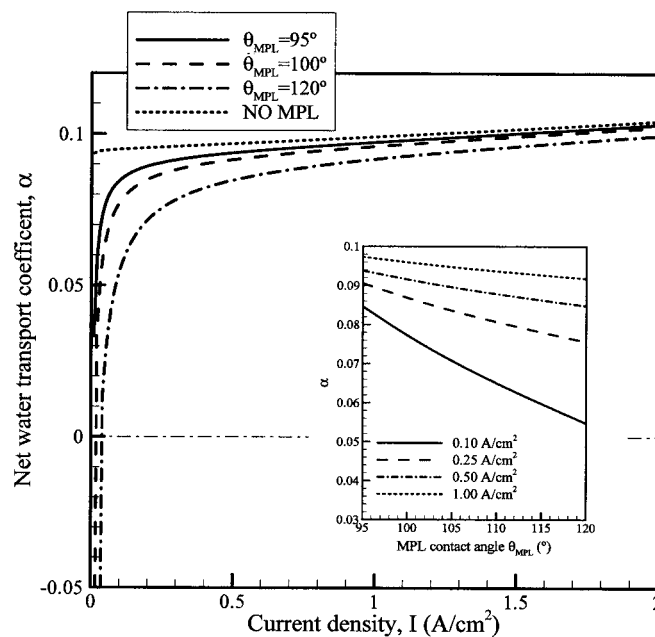
Conclusions

A one-dimensional, two-phase model has been developed for bilayer GDMs and membrane of a PEFC, and the effects of the MPL and its properties on water transport are analyzed. The following conclusions can be drawn from this study:

(1) Bilayer cathode GDM provides better water management capability, particularly by increasing the tendency of water flow toward the anode. This effect is a consequence of the hydraulic pressure build-up due to strong capillary pressure in MPL and the increased resistance to liqued water removal from the cathode. This, in turn, establishes a higher pressure differential across the membrane, promoting the transport of water from cathode to anode by permeation.

(2) The reduced water flux toward the cathode decreases cathode flooding; therefore, it improves the cell performance by relaxing the mass transfer limitations. Furthermore, a discontinuity in the liquid saturation profile at the MPL and GDL interface arises due to their differing microporous and wetting characteristics. This discontinuity further reduces the flooding in the cathode catalyst layer-MPL interface, particularly when saturation levels at the GDL-channel interface are high.

(3) It is seen that the water flux toward the anode is enhanced with smaller pore size, larger thickness and hydrophobicity, and lower porosity of the MPL.

Although we have not considered an MPL in the anode GDM, it is expected that the effect of the anode MPL may not be significant unless the anode is as severely flooded as the cathode.

The gas-phase transport and electron transport are also affected by the MPL pore structure and wetting characteristics, so they need to be accounted for in the MPL optimization. Work is underway to analyze these effects to further optimize the MPL pore structure and its wetting characteristics.

List of Symbols

C^i	molar concentration of species i, mol/m^3
d	pore diameter of MPL, μm
d_h	hydraulic diameter of the channel, m
D^i	diffusion coefficient of species i, m^2/s
EW	equivalent weight of membrane, 1.1 kg/mol for Nafion 11-
F	Faraday's constant, 96 487 C/mol
h_m	convective mass transfer coefficient, m/s
I	current density, A/m^2
$\mathbf{j}_k$	mass flux of phase k, kg/(m^2/s)
$\mathbf{K}$	absolute permeability, m^2
k_{rk}	relative permeability of phase k
M^i	molecular weight of species i, kg/mol
p	pressure, Pa
s	liquid saturation
$\mathbf{u}$	velocity, m/s

Subscripts

c	capillary
g	gas
int	interface
l	liquid
m	membrane
sat	saturation

Superscripts

GDL	gas diffusion layer
MPL	microporous layer
H$_2$O	water species
O$_2$	oxygen species

Greek

α	net water transport coefficient
δ	thickness
ε	bulk porosity
γ_c	advection coefficient
λ	water content of membrane (#H$_2$O/#SO$_3$H)
λ_k	relative mobility of phase k
μ	dynamic viscosity, Pa/s
ν	kinematic viscosity, m^2/s
ρ	density, kg/m^3
ρ_{dry}	dry density of membrane, kg/m^3
σ	surface tension, N/m
θ_c	contact angle,°

References

1. M. S. Wilson, J. A. Valerio, and S. Gottesfeld, *Electrochim. Acta*, **40**, 355 (1995).
2. N. Hara, K. Tsurumi, and M. Watanabe, *J. Electroanal. Chem.*, **413**, 81 (1996).
3. E. Passalacqua, F. Lufrano, G. Squadrito, A. Patti, and L. Giorgi, *Electrochim. Acta*, **43**, 3665 (1998).
4. V. A. Paganin, E. A. Ticianelli, and E. R. Gonzales, *J. Appl. Electrochem.*, **26**, 297 (1996).
5. Z. Qi and A. Kaufman, *J. Power Sources*, **109**, 38 (2002).
6. C. S. Kong, D-Y. Kim, H-K. Lee, Y-G. Shul, and T-H. Lee, *J. Power Sources*, **108**, 185 (2002).
7. L. R. Jordan, A. K. Shukla, T. Behrsing, N. R. Avery, B. C. Muddle, and M. Forsyth, *J. Appl. Electrochem.*, **30**, 641 (2000).
8. G. J. M. Jannsen and M. L. J. Overvelde, *J. Power Sources*, **101**, 117 (2001).
9. E. Passalacqua, G. Squandrito, F. Lufrano, A. Patti, and L. Giorgi, *J. Appl. Electrochem.*, **31**, 449 (2001).
10. L. Giorgi, E. Antolini, A. Pozio, and E. Passalacqua, *Electrochim. Acta*, **43**, 3675 (1998).
11. I. Cabasso, Y. Yuan, and X. Xu, U.S. Pat. 5,783,325 (1998).
12. S. J. Lee, S. Mukarjee, J. McBreen, Y. W. Rho, Y. T. Kho, and T. H. Lee, *Electrochim. Acta*, **43**, 3693 (1998).
13. H. H. Voss, D. P. Wilkinson, P. G. Pickup, M. C. Johnson, and V. Basura, *Electrochim. Acta*, **40**, 321 (1995).
14. J. H. Nam and M. Kaviany, *Int. J. Heat Mass Transfer*, **46**, 4595 (2003).
15. U. Pasaogullari and C. Y. Wang, *Abstract No. 1103, 204th Electrochemical Society Meeting*, Oct. 12-16, 2003, Orlando, FL.
16. U. Pasaogullari and C. Y. Wang, *Electrochim. Acta*, **49**, 4359 (2004).
17. U. Pasaogullari and C. Y. Wang, *J. Electrochem. Soc.*, **151**, A399 (2004).
18. A. Weber and J. Newman, *Abstract No. 1038, 204th Electrochemical Society Meeting*, Oct. 12-16, 2003, Orlando, FL.
19. A. Weber and J. Newman, *Chem. Rev. (Washington, D.C.)*, **104**, 4679 (2004).
20. C. Y. Wang, *Chem. Rev. (Washington, D.C.)*, **104**, 4727 (2004).
21. U. Pasaogullari and C. Y. Wang, *Abstract No. 1190, 203rd Electrochemical Society Meeting*, April 27-May 2, 2003, Paris, France.
22. U. Pasaogullari and C. Y. Wang, *J. Electrochem. Soc.*, **152**, A380 (2004).
23. C. Y. Wang and P. Cheng, *Adv. Heat Transfer*, **30**, 93 (1997).
24. Z. H. Wang and C. Y. Wang, *J. Power Sources*, **94**, 40 (2001).
25. W. He, J. S. Yi, and T. V. Nguyen, *AIChE J.*, **46**, 2053 (2000).
26. D. Natarajan and T. V. Nguyen, *J. Electrochem. Soc.*, **148**, A1324 (2001).
27. R. E. Meredith and C. W. Tobias, in *Advances in Electrochemical Science and Engineering*, 2nd ed., C. W. Tobias, Editor, Interscience New York (1962).
28. T. A. Zawodzinski, T. E. Springer, F. Uribe, and S. Gottesfeld, *Solid State Ionics*, **60**, 199 (1993).
29. D. M. Bernardi and M. W. Verbrugge, *J. Electrochem. Soc.*, **139**, 2477 (1992).
30. F. Meier and G. Eigenberger, *Electrochim. Acta*, **49**, 1731 (2004).
31. S. Motupally, J. A. Becker, and J. W. Weidner, *J. Electrochem. Soc.*, **147**, 3171 (2000).
32. T. E. Springer, T. A. Zawodzinski, and S. Gottesfeld, *J. Electrochem. Soc.*, **138**, 2334 (1991).
33. T. A. Zawodzinski, J. Davey, J. Valerio, and S. Gottesfeld, *Electrochim. Acta*, **40**, 297 (1995).
34. X. G. Yang, F. Y. Zhang, A. L. Lubawy, and C. Y. Wang, *Electrochem. Solid-State Lett.*, **7**, A408 (2004).
35. M. Kaviany, *Principles of Heat Transfer in Porous Media*, Springer, New York (1999).
36. P. D. Beattie, V. I. Basura, and S. Holdcroft, *J. Electroanal. Chem.*, **468**, 180 (1999).
37. F. P. Incropera and D. P. DeWitt, *Fundamentals of Heat and Mass Transfer*, Wiley, New York (1996).
38. M. V. Williams, H. R. Kunz, and J. M. Fenton, *J. Electrochem. Soc.*, **151**, A1617 (2004).